

4A.4 THE IMPORTANCE OF RESOLVED MICROPHYSICS TO REINTENSIFICATION DURING THE EXTRATROPICAL TRANSITION OF TROPICAL CYCLONES

Brian J. Gaudet and Elizabeth A. Ritchie *
University of New Mexico, Albuquerque, New Mexico.

1. INTRODUCTION

The extratropical transition of tropical cyclones (hereafter TCs) can be a particularly complex process (e.g. DiMego and Bosart 1982; Harr and Elsberry 2000; Klein et al. 2000; Jones et al. 2003). As a general outline, however, as they progress northward they undergo what Klein et al. (2002) refer to as the transformation stage, which involves the loss of axisymmetry, an upper-level warm core, and other characteristics. However, if the TC remnant is able to interact with an upper-level system, a reintensification stage may then occur, and the system may become a potent extratropical cyclone.

In order to learn more about the reintensification stage, an idealized study was performed using the An idealized modeling study (Ritchie and Elsberry 2003) was performed using the COAMPS[®] regional model¹. A series of simulations was performed, each containing a low-level TC-like vortex and an upper-level trough of various strengths. It was found that, whereas the trough-induced minimum sea level pressure (SLP) was dependent on the strength of the trough, the minimum SLP of the reintensified TC remnant was almost insensitive to trough strength (and in all cases lower than that achieved in the trough-only simulations).

Recently other idealized simulations have been performed to investigate the role of the trough/TC spatial configuration. In this case it was found that reintensification was highly sensitive to the details of the initial configuration (Ritchie 2005).

All of the preceding simulations were performed using 27 km grid spacing on the finest, or only, grid. In this study increased resolution will be introduced into the simulations to allow a closer examination of the reintensification process, and in particular the role of resolved microphysical processes.

2. NUMERICAL MODEL

COAMPS is a nonhydrostatic, parallel-processing regional model that allows one-way interactive nested grids, which may move relative to the parent grid. The model may be run in either a real data or idealized mode. Convection is parameterized by a Kain-Fritsch scheme (Kain

and Fritsch 1993) for horizontal grid spacings over a certain threshold; explicit microphysics is performed on all grids. The standard microphysics scheme is based on the single moment bulk method found in Rutledge and Hobbs (1983, 1984); the mixing ratios of cloud water, rain, pristine ice, snow, and graupel are predicted. However, in a previous version of the microphysics only the snow category was present. More information about the model can be found in Hodur (1997).

For the COAMPS standard microphysics, the hydrometeor collection interactions considered are rain collecting snow, snow collecting rain, graupel collecting snow, and graupel collecting rain. In the absence of melting or shedding, and provided hydrometeor amounts exceed certain thresholds, the destination category for all these interactions is graupel. When graupel is excluded, snow becomes the destination category for riming.

3. SIMULATION OVERVIEW

The simulations were designed to be idealized. The initial condition consisted of a superposition of an idealized upper-level trough and a TC, as described in Ritchie and Elsberry (2003). (Figures 1 and 2). The relative position of the trough and TC could be varied by 10° increments in longitude and 5° increments in latitude. The coarse grid configuration was the same as used in Gaudet and Ritchie (2005), namely 319 × 337 × 36 with 27 km horizontal grid spacing. A horizontal climatological SST distribution and surface fluxes were used, but no land surfaces were present in the simulations. (Political boundaries are left in the figures for spatial reference).

An initial set of simulations was performed without nesting, and without graupel (all simulations were performed without graupel unless otherwise specified). The TC was seen to progress northward and transform into an extratropical system as a surface baroclinic wave develops. The transformed TC either gradually decayed or reintensified, depending on the initial trough/TC spatial configuration. In either case, the location of the SLP minimum corresponding to the remnant TC was tracked.

A new set of simulations was then performed using nested grids; Grid 2 was 136 × 136 with 9 km spacing while Grid 3 was 199 × 199 with 3 km spacing. Grid 2 moved to follow the track of the pressure minimum in the corresponding single-grid simulation. This procedure does not keep the Grid 2 SLP minimum precisely at the grid center, but subsequent radial analyses are always done with respect to the actual remnant TC SLP minimum location. Grid 3 is concentric with and follows Grid 2.

It was found that the 10S25E and 10S35E simula-

*Corresponding author address: Brian J. Gaudet, Department of Electrical and Computer Engineering, 1 University of New Mexico, Albuquerque, NM 87131; e-mail: bgaudet@ece.unm.edu.

¹COAMPS[®] is a registered trademark of the Naval Research Laboratory in Monterey, CA.

tions bracket the boundary between reintensifying and non-reintensifying cases (Ritchie 2005). (The designation 10S25E means that the TC is initially 10 degrees south and 25 degrees east of the trough.) In the single-grid simulations the former began to reintensify after 48 hr, while the latter approached a near steady-state and then gradually weakened over time (Figure 3). We now focus on the relative evolution of these two cases in the nested simulations.

4. LOW-LEVEL VORTICITY

A look at the low-level vorticity evolution in the 10S25E case reveals that, by the time of maximum SLP at 45 hr, while the initial vorticity (not shown) has weakened considerably, it is still concentrated in a quasi-circular vortex (Figure 4). Vorticity in the northern part of the grid is associated with the approaching baroclinic zone, as can be seen in the virtual potential temperature fields at 51 hr (Figure 5). Also apparent in Figure 5 is the warm, moist air being wrapped cyclonically around the remnant TC, and confined to an increasingly narrow band to the south of the baroclinic zone.

As the frontal vorticity approaches and reaches the location of the TC remnant, the location of maximum vorticity suddenly switches to a narrow band of vorticity aligned with the frontal zone (Figure 6). This occurs at approximately 57 hr, during a period of rapid decrease of SLP (4.5 mb in 6 hr). The vorticity band appears to subsume the TC remnant vorticity and continues to increase in intensity (Figure 7), as a remnant concentration of frontal vorticity passes to the south. Eventually the maximum vorticity magnitude decreases again, but the SLP minimum continues to intensify. Minimum SLP occurs when vorticity is again wrapped into a localized quasi-circular region (Figure 8).

In the 10S35E case, the vorticity structure at 54 hr is similar to the 10S25E case (Figure 9). What is different is that the pressure is continuing to rise (albeit slowly). Also, when the TC remnant encounters the warm front of the developing baroclinic wave, the front has a NW-to-SE orientation. Finally, the cold front of the developing wave is also interacting with the TC remnant on its west side. A jump in the maximum vorticity to a discrete vorticity band does occur at 72 hr (Figure 10). However, the vorticity magnitude does not become quite as large (to $5.5 \times 10^{-4} \text{ s}^{-1}$), the pressure decreases only slightly, and there appears to be no tendency for the vorticity to become concentrated again (Figure 11).

5. THERMAL ADVECTION VERTICAL FORCING

It has been suggested in the past that reintensification of TC remnants can be associated with the influence of thermal advection in Petterssen Type B frontogenesis (DiMego and Bosart 1982). We now briefly outline the process involved on the synoptic scale, and attempt to infer behavior on slightly smaller scales.

For simplicity, and based on Davies-Jones (1991), we assume the form of hydrostatic balance $\partial\Phi/\partial Z = b$, where Φ is geopotential, $b = g\theta_v/\theta_{v0}$ is buoyancy, and $Z = c_p T_0 [1 - (p/p_0)^{R/c_p}]/g$ is pseudoheight, which corresponds to actual height in an adiabatic atmosphere (Hoskins and Bretherton 1972). Hence, if hydrostatic balance is assumed, then $\nabla_H^2 b - \partial(\nabla_H^2 \Phi)/\partial Z = 0$. The local tendency of this quantity can be obtained by taking ∇_H^2 of db/dt and $\partial/\partial Z$ of $d(\nabla_H^2 \Phi)/dt$. If we assume the flow is approximately 2D incompressible, inviscid, f -plane, adiabatic, and initially hydrostatic, we can use $db/dt = 0$ to obtain:

$$\frac{\partial}{\partial t} \left[\nabla_H^2 b - \frac{\partial}{\partial Z} (\nabla_H^2 \Phi) \right] = \overbrace{\frac{\partial v_i}{\partial Z} \frac{\partial}{\partial x_i} (\nabla_H^2 \Phi)}^A - \overbrace{\frac{\partial b}{\partial x_i} \frac{\partial^2 v_i}{\partial x_i \partial x_i}}^B - \overbrace{2 \frac{\partial v_i}{\partial x_j} \frac{\partial^2 b}{\partial x_j \partial x_i}}^C - \overbrace{\frac{\partial}{\partial Z} \left[\frac{d_N}{dt} (\nabla_H^2 \Phi) \right]}^D, \quad (1)$$

where we have reverted to Einstein summation notation on the RHS, and d_N/dt is a material derivative following nondivergent flow.

Term A (1) derives from the vertical derivative of the $\nabla_H^2 \Phi$ equation, which in the quasigeostrophic (QG) framework is $f_0 \zeta_r$, where ζ_r is the relative vorticity. Considered in isolation, it represents a local tendency in $\partial \nabla_H^2 \Phi / \partial Z$ without the corresponding hydrostatic tendency in $\nabla_H^2 b$. Term B in (1) derives from the Laplacian of the b equation; in the QG regime it is actually equal to the first term by the thermal wind relation, and the two combine to produce the thermal wind vorticity advection term in the QG omega equation of Trenberth (1978). Term C also derives from the b equation, and corresponds to the deformation function of the QG omega equation described by Wiin-Nielsen (1959). It is this term we will consider further. In isolation, it represents a local tendency in $\nabla_H^2 b$ without the corresponding hydrostatic tendency in $\partial(\nabla_H^2 \Phi)/\partial Z$. The last term in (1) is zero in the QG regime because the material derivative reduces to $f_0 d_N(\zeta_r)/dt$, which is zero.

If the terms on the RHS of do not cancel, hydrostatic balance cannot be maintained, and vertical motion and/or divergent motion will generated, eventually restoring balance.

For scales smaller than a few hundred kilometers QG theory is not formally valid. However, from the arguments above, we can still expect that the deformation function in (1) will lead to upward vertical forcing when negative. In fact, it was noted by Wiin-Nielsen (1959) that the geostrophic version of Term C generally occurs on a smaller scale than that of thermal wind vorticity advection. If the axis of dilatation of the horizontal wind field is Θ_v , and Θ_b is defined as the axis of dilatation of the field $\nabla_H b$, then the deformation function leads to vertical motion when $|\Theta_b - \Theta_v| < \pi/4$. If $\nabla_H b$ only changes in the direction of $\nabla_H b$ (i.e., a 1D baroclinic zone), then this term corresponds to the convergence of the vector frontogenesis function, which has been shown to lead to vertical motion on the frontal scale, with ascent on the warm

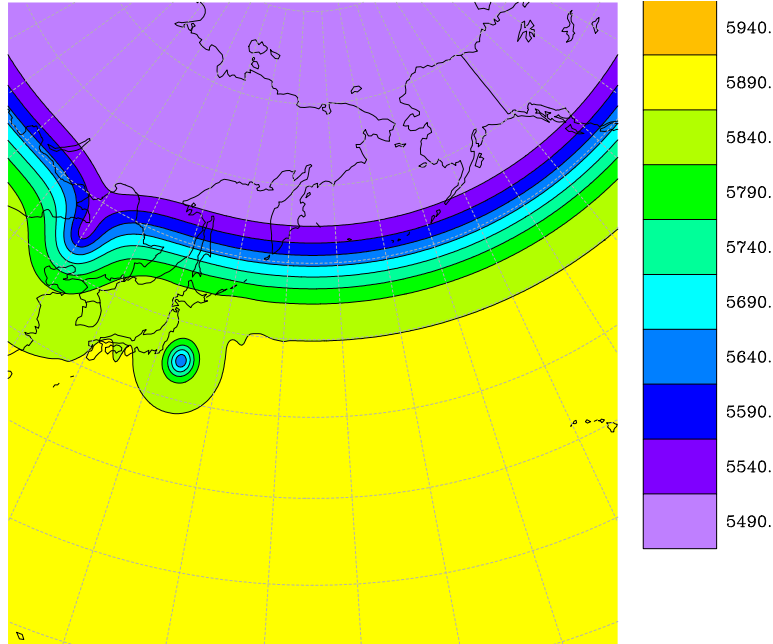


Figure 1: Geopotential heights (m) at 500 mb on Grid 1 for 10S25E model initialization.

side of the front (Keyser et al. 1988). In a QG framework, such vertical motion would restore hydrostatic and geostrophic balance through a combination of converging low-level vorticity at the expense of upper-level vorticity, and adiabatic cooling.

6. APPLICATION TO SIMULATIONS

We thus find that the formation of a low-level extended strip of vorticity along the warm side of a frontal zone is just what we would expect from a consideration of the deformation function lift. More specifically, the vorticity should be associated with a horizontally-narrow local maximum of buoyancy. Finally, if the characteristics of this vorticity strip are critical to reintensification, then the characteristics of the buoyancy strip should be critical as well.

First, we consider the effect of the TC remnant on the low-level buoyancy field. When a large-scale vortex is present, horizontal isentropes are distorted, and vertical motion from the buoyancy Laplacian term generally occurs in the warm sector of an intensified baroclinic zone (Keyser et al. 1988; Klein et al. 2000). One way to consider the effect of the vortex is to examine its deformation. If the radial wind field v_r is zero and the tangential wind field $v_\theta = v_\theta(r) > 0$ is decreasing with radius, then the axis of dilatation induced by the circulation is directed 45° to the left of the wind. Hence gradients of scalars tend to be rotated towards this direction (Keyser et al. 1988; Bluestein 1993; Harr and Elsberry 2000). For a northern hemispheric cyclonic vortex in a north-south buoyancy gradient, one would expect maximum buoyancy

Laplacian vertical motion in the NE quadrant.

Ritchie (2005) found a number of parameters that were able to separate reintensifying and non-reintensifying cases prior to the time of maximum pressure. Among these were NE quadrant precipitation within 600 km radius (rates exceeding 2.3 mm in 6 h indicated reintensification). Another such parameter was NW quadrant precipitation (rates exceeding 0.6 mm in 6 h), but this tended to occur closer to the center than the NE quadrant precipitation. It was noted that the arc-like shape of the precipitation field was consistent with being co-located with the warm front associated with TC circulations.

In our 10S25E reintensifying simulation we can see just this curved structure in the structure of the bands of model rain rate. There are actually two bands of rain apparent at 48 h (Figure 12): one associated with the TC remnant, the other associated with the approaching front. The merger of these bands, and the pinching off of the warm strip between them, coincides with the intensification of the low-level vorticity band (Figure 13 and 14).

Figure 15 shows a trace of the area-averaged rain rate on Grid 2 within a 600 km radius of the TC remnant pressure center, as well as the averaged rain rates within the NE and NW quadrants of this region. This plot confirms that prior to reintensification the rain rate increases significantly, preferentially in the NW quadrant and even more preferentially in the NE quadrant. In fact, it can be seen that the peak in rain rate occurs at the same time as the previously-described low-level vortex jump and rainband merger; afterwards the rain rate in the northern quadrants decrease as rapidly as they had increased.

In the 10S35E simulation, there are also both a

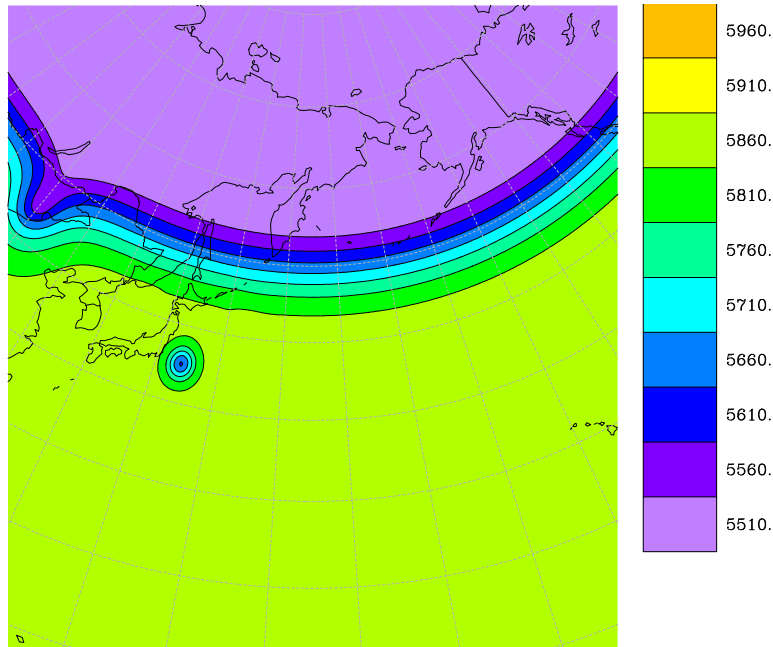


Figure 2: Same as Figure 1, but for 10S35E model initialization.

precipitation shield associated with the TC remnant and frontal rain bands in the NE quadrant, and their merger also coincides with the formation of the low-level vorticity band. But the structure of the precipitation bands is less well organized and does not result in the arc structure expected from vortex deformation (Figure 16). A trace of the rain rate (Figure 17) again shows NE quadrant rain increasing dramatically until the time of the low-level vortex jump. The main differences from the 10S25E case are: 1) the absolute values of the rain rates are lower, and 2) the NW quadrant average rain rate is about the same as the total area average rain rate, whereas in the developing 10S25E case the NW quadrant rate is considerably more than the total area rate. This may be a reflection of the fact that the TC remnant in the 10S35E case has not been able to concentrate low-level moist air into the optimal arc shape.

Grid 3 is not sufficiently large to capture the full structure of the NE quadrant rainbands, but we can use it to examine the structure of the NW quadrant rainbands, which occur closer to the TC remnant center. Figure 18 shows that the average rain rate of Grid 3 within 250 km of the center is nearly identical for the 10S25E and 10S35E simulations, but the average rain rate in the NW quadrant of this region is far greater in the reintensifying case than in the non-reintensifying one. For this particular case, however, this signal does not become apparent until shortly before the vorticity jump, approximately 6 hours after the minimum SLP has already begun to decrease.

An additional distinction of the 10S35E simulation is the presence of localized vorticity along the cold front while the vorticity band is being concentrated along the

warm front (see Figure 6), whose strain may be preventing the final concentration of a reintensified vortex and a more rapid reduction in pressure. It is not clear yet whether the absence of vorticity re-concentration has more to do with the presence of cold frontal vorticity or with the suboptimal configuration and strength of warm frontal vorticity; further investigation into this process is planned.

To summarize, it appears from this case comparison that reintensification of the TC remnant is related to the uplift associated with a favorable superposition of the frontogenetical function of the TC remnant circulation and the baroclinic zone that it approaches. Harr and Elsberry (2000) also had stressed the importance of the frontogenetical function caused by the interaction of a vortex and the large-scale environment. The resultant uplift is seen to intensify a low-level band of frontal vorticity until it subsumes the low-level vorticity of the TC remnant, but during reintensification this vorticity collapses back into a closed circulation.

7. MICROPHYSICAL SENSITIVITY

Because of the apparent importance of thermal advection to the evolution of the low-level vorticity, and because of the correlation between NE quadrant precipitation and reintensification, we investigated the sensitivity of the system's evolution to the microphysics scheme. Specifically, we examined the influence of adding the graupel category.

In Figure 19, we show the area-averaged column-integrated ice-phase hydrometeor mass (graupel plus

snow) in the NE quadrant of the 10S25E case (within 600 km radius). Though the difference is hardly noticeable for the 27 km Grid 1, it can temporarily reach 30% for the 9 km Grid 2. The snow simulation produces more ice hydrometeors in this region. However, the area-averaged column-integrated rain mass for the same region shows virtually no difference between the graupel and snow-only simulations, and there is likewise little variation in the rain rate.

Furthermore, no significant differences were found in the dynamical evolution of the storms between the graupel and snow-only simulations. at any grid spacing (Figure 20). This is consistent with some recent results from CAMEX (e.g. Hausman et al. (2006)) which indicate the sensitivity of modeled mature tropical cyclones to ice diabatic heating is rather small, though the sensitivity to hydrometeor fall velocity was greater. This would also seem to be consistent with our finding that the vorticity concentration seems to be a low-level process. The effects of differential hydrometeor fall velocity may become more significant one horizontal grid spacings reach the kilometer scale.

8. CONCLUSION

With finer resolution, the reintensification process was seen to be associated with the convergence of warm frontal vorticity induced by thermal advection, which then interacts with the vorticity of the parent TC remnant. In reintensification the vorticity becomes concentrated again into a compact region, whereas in a non-reintensifier the vorticity remained extended. The key difference appeared to be the presence of an optimal warm frontal configuration and the absence of interaction with the cold front; this interaction leads to a characteristic arc in the precipitation field. The change of ice microphysics, however, had little effect on the evolution, probably because the mixing ratios of ice were too low, and because the evolution appears to have initiated at low levels. It is possible that the sensitivity to microphysics scheme would be much enhanced for resolutions at which convective cells are explicitly resolved. Future work will investigate sensitivity at this scale, as well as to elucidate the nature of the vorticity interaction that leads to the concentrated vortex of the reintensified TC remnant. It will also be determined to what extent this evolution can be generalized to the whole set of TC/trough interaction cases.

9. ACKNOWLEDGMENTS

This research was performed under grant #N00014-03-1-0831 of the Office of Naval Research Marine Meteorology Program. All simulations were performed at the Albuquerque Center for High Performance Computing and Education.

REFERENCES

- Bluestein, H.B., 1993: *Synoptic-Dynamic Meteorology in Midlatitudes. Volume II: Observations and Theory of Weather Systems*. Oxford University Press, 594 pp.
- Davies-Jones, R., 1991: The frontogenetical forcing of secondary circulations. Part I: The duality and generalization of the Q vector. *J. Atmos. Sci.*, **48**, 497-509.
- DiMego, G.J., and L.F. Bosart, 1982: The transformation of tropical storm Agnes into an extratropical cyclone. Part II: Moisture, vorticity, and kinetic energy budgets. *Mon. Wea. Rev.*, **110**, 412-433.
- Gaudet, B.J., and E.A. Ritchie, 2005: Relationships between mixed-phase microphysical collection and modeled precipitation in various regimes. *11th Conference on Mesoscale Processes*, American Meteorological Society, 24 Oct – 28 Oct 2005, Albuquerque, NM CD-ROM, P1M.12.
- Harr, P.A., and R.L. Elsberry, 2000: Extratropical transition of tropical cyclones over the western North Pacific. Part I: Evolution of structural characteristics during the transition process. *Mon. Wea. Rev.*, **128**, 2613-2633.
- Hausman, S.A., K.V. Ooyama, and W.H. Schubert, 2006: Potential vorticity structure of simulated hurricanes. *J. Atmos. Sci.*, **63**, 87-108.
- Hodur, R.M, 1997: The Naval Research Laboratory's Coupled Ocean/Atmosphere Mesoscale Prediction System (COAMPS). *Mon. Wea. Rev.*, **125**, 1414-1430.
- Hoskins, B.J., and F.P. Bretherton, 1972: Atmospheric frontogenesis models: Mathematical formulation and solution. *J. Atmos. Sci.*, **29**, 11-37.
- Jones, S.C., and coauthors, 2003: The extratropical transition of tropical cyclones: Forecast challenges, current understanding, and future directions. *Wea. Forecasting*, **18**, 1052-1092.
- Keyser, D., M.J. Reeder, and R.J. Reed, 1988: A generalization of Petterssen's frontogenesis function and its relation to the forcing of vertical motion. *Mon. Wea. Rev.*, **116**, 762-780.
- Klein, P.M., P.A. Harr, and R.L. Elsberry, 2000: Extratropical transition of western North Pacific tropical cyclones: An overview and conceptual model of the transformation stage. *Wea. Forecasting*, **15**, 373-395.
- Ritchie, E.A., 2005: Simulated precipitation structure of the extratropical transition of tropical cyclones. *11th Conference on Mesoscale Processes*, American Meteorological Society, 24 Oct – 28 Oct 2005, Albuquerque, NM, CD-ROM, P6M.4.

- Ritchie, E.A., and R.L. Elsberry, 2003: Simulations of the extratropical transition of tropical cyclones: Contributions by the midlatitude upper-level trough to reintensification. *Mon. Wea. Rev.*, **131**, 2112-2128.
- Rutledge, S.A., and P.V. Hobbs, 1983: The mesoscale and microscale structure of organization of clouds and precipitation in midlatitude cyclones. VIII: A model for the "seeder-feeder" process in warm-frontal rainbands. *J. Atmos. Sci.*, **40**, 1185-1206.
- Rutledge, S.A., and P.V. Hobbs, 1984: The mesoscale and microscale structure of organization of clouds and precipitation in midlatitude cyclones. XII: A diagnostic modeling study of precipitation development in narrow cold-frontal rainbands. *J. Atmos. Sci.*, **41**, 2949-2972.
- Trenberth, K.E., 1978: On the interpretation of the diagnostic quasi-geostrophic omega equation. *Mon. Wea. Rev.*, **106**, 131-137.
- Wiin-Nielsen, A., 1959: On a graphical method for an approximate determination of the vertical velocity in the mid-troposphere. *Tellus*, **11**, 432-440.

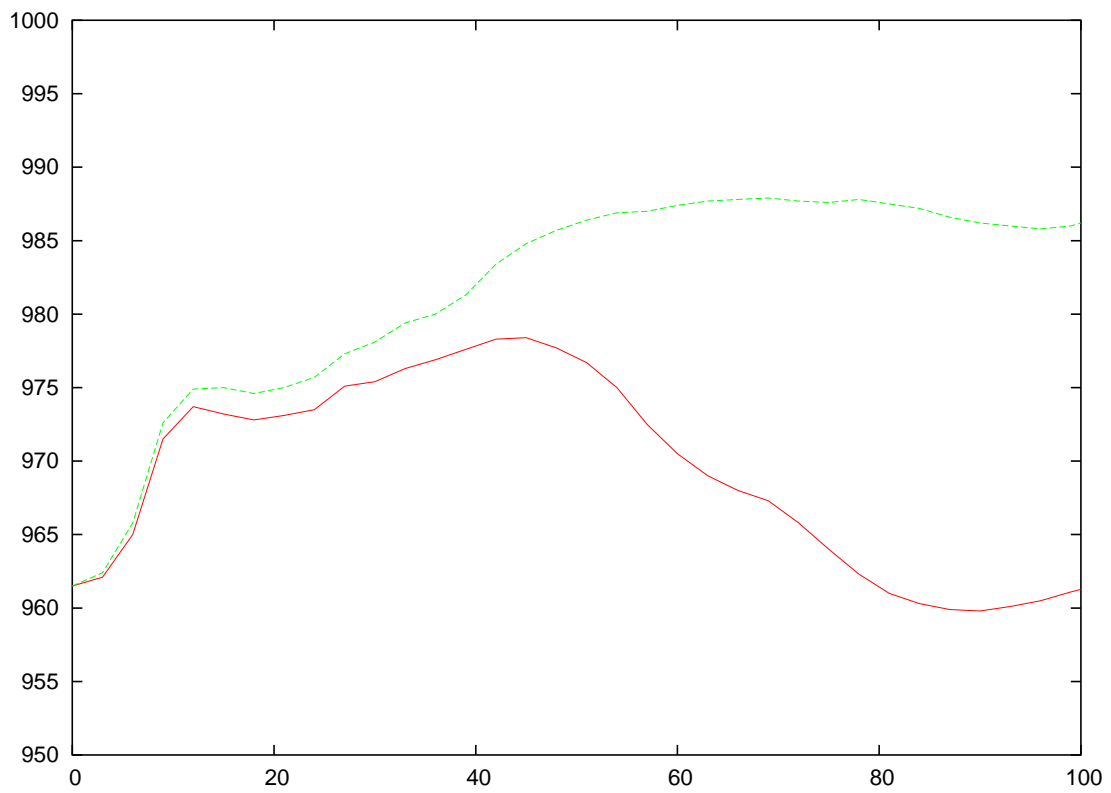


Figure 3: Minimum surface pressure of TC remnant vs. time for single grid 10S25E (red) and 10S35E (green) simulations.

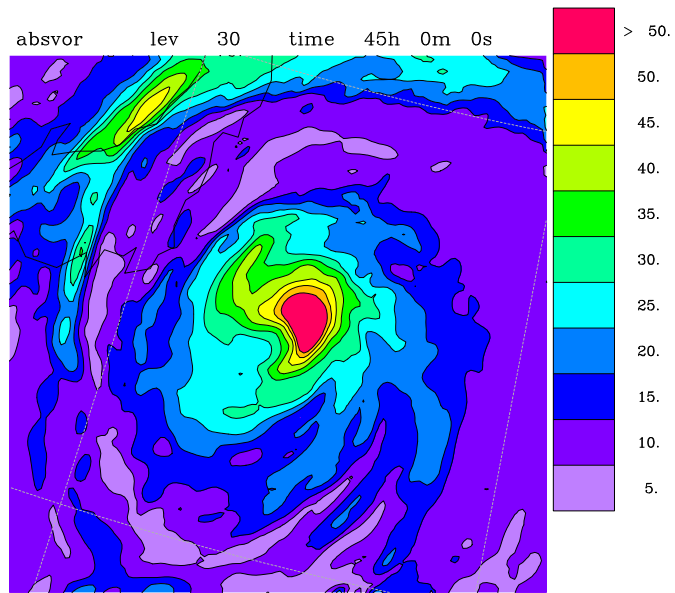


Figure 4: Absolute vorticity (10^{-5}s^{-1}) for 275 m above surface on Grid 2 at 45 hr during 10S25E simulation.

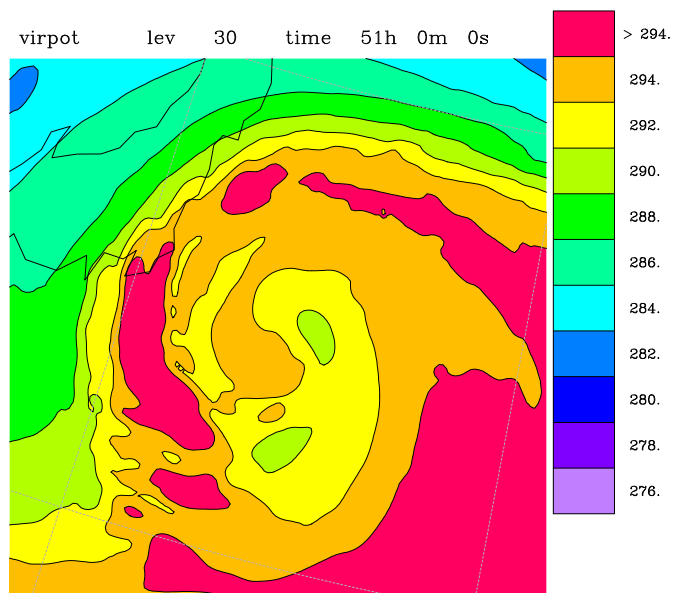


Figure 5: Virtual potential temperature (K) for 275 m above surface on Grid 2 at 51 hr during 10S25E simulation.

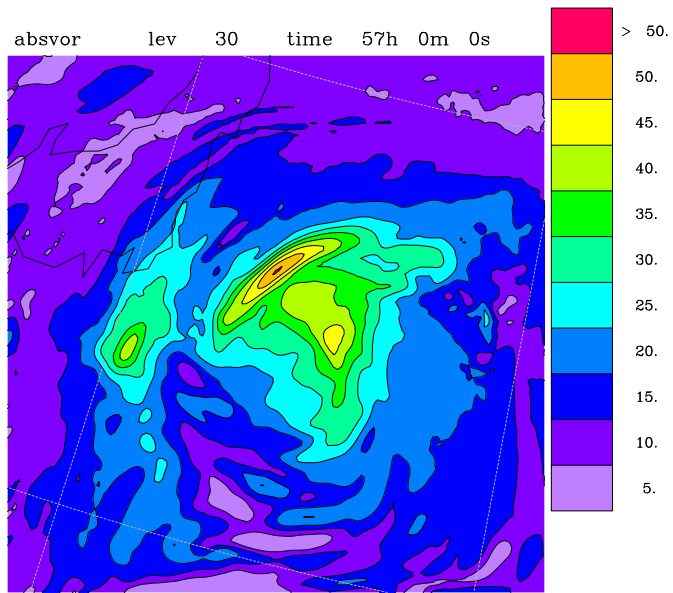


Figure 6: Same as Figure 4, but at 57 hr.

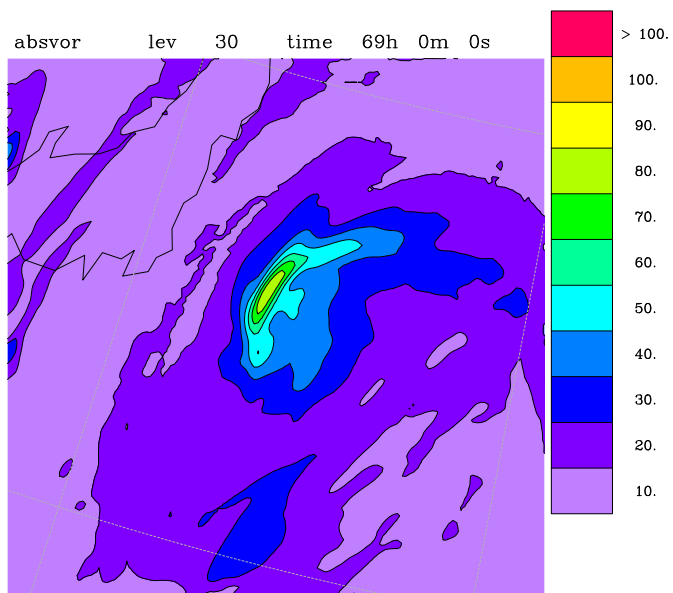


Figure 7: Same as Figure 4, but at 69 hr. Note the different color shading increment.

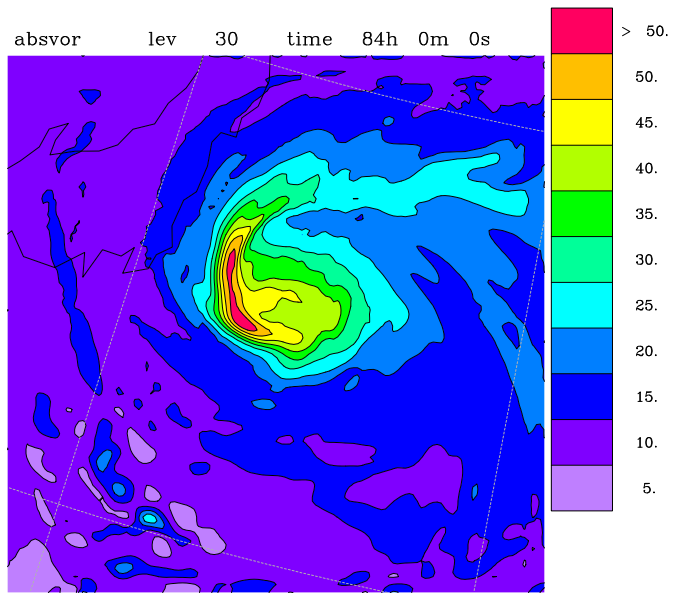


Figure 8: Same as Figure 4, but at 84 h.

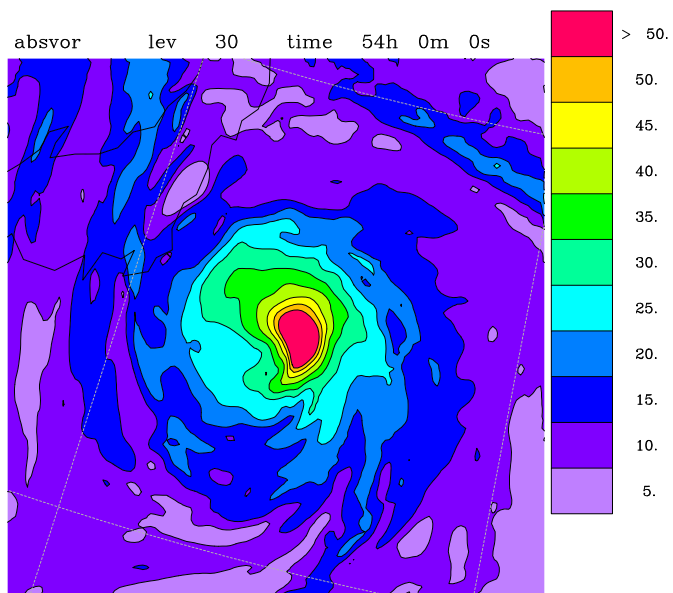


Figure 9: Same as Figure 4, but at 54 hr during 10S35E simulation.

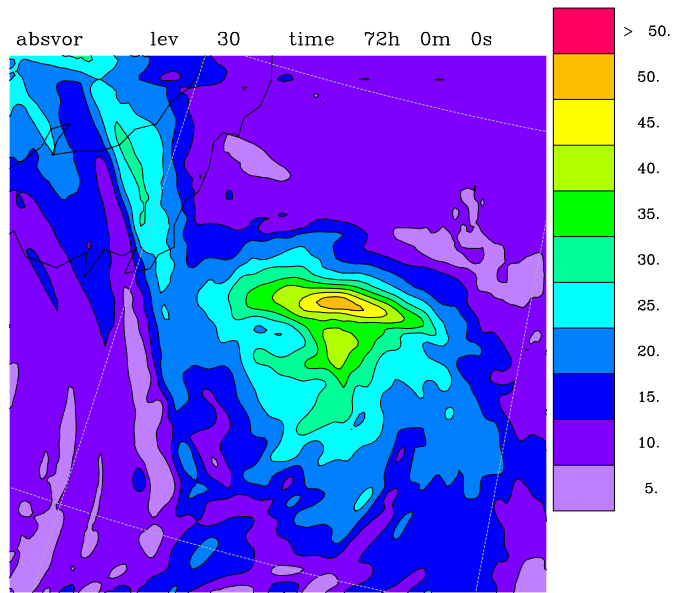


Figure 10: Same as Figure 9, but at 72 hr.

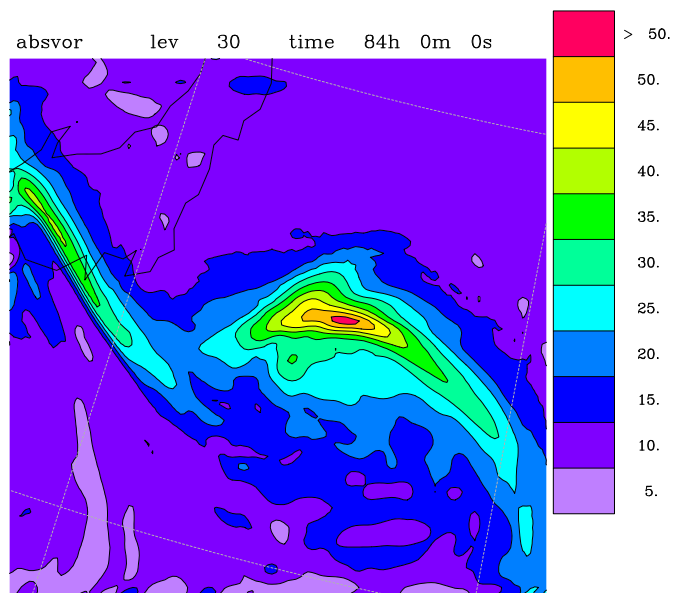


Figure 11: Same as Figure 9, but at 84 hr.

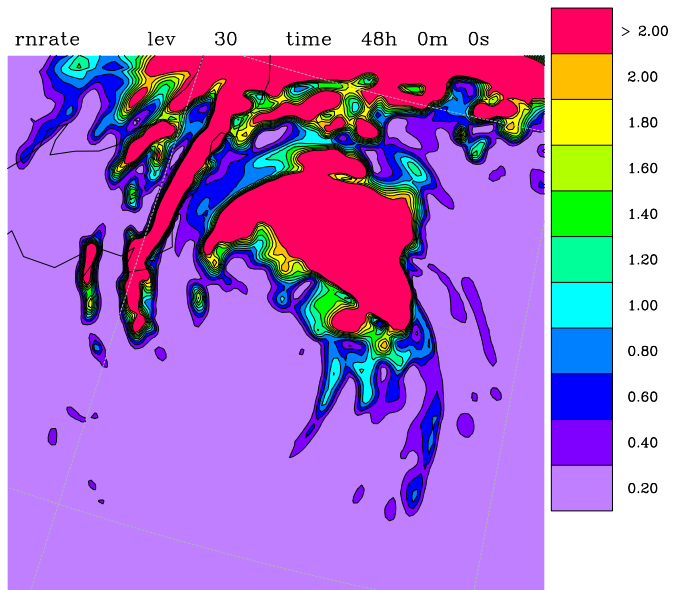


Figure 12: Model rain rate (mm hr⁻¹) for 10S25E simulation on Grid 2 at 48 hr.

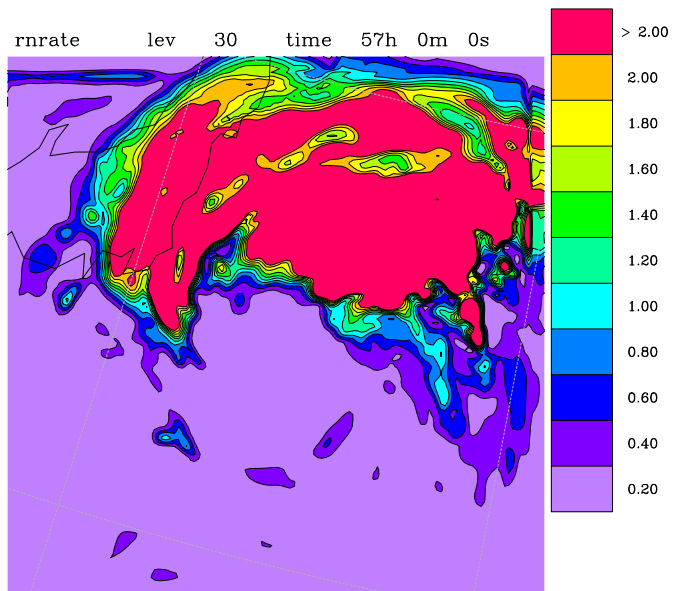


Figure 13: Same as Figure 12, but at 57 hr.

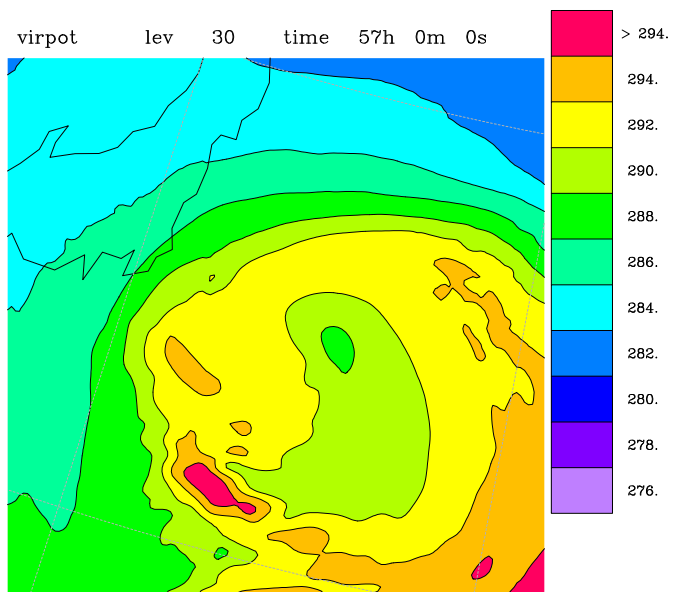


Figure 14: Same as Figure 5, but at 57 hr.

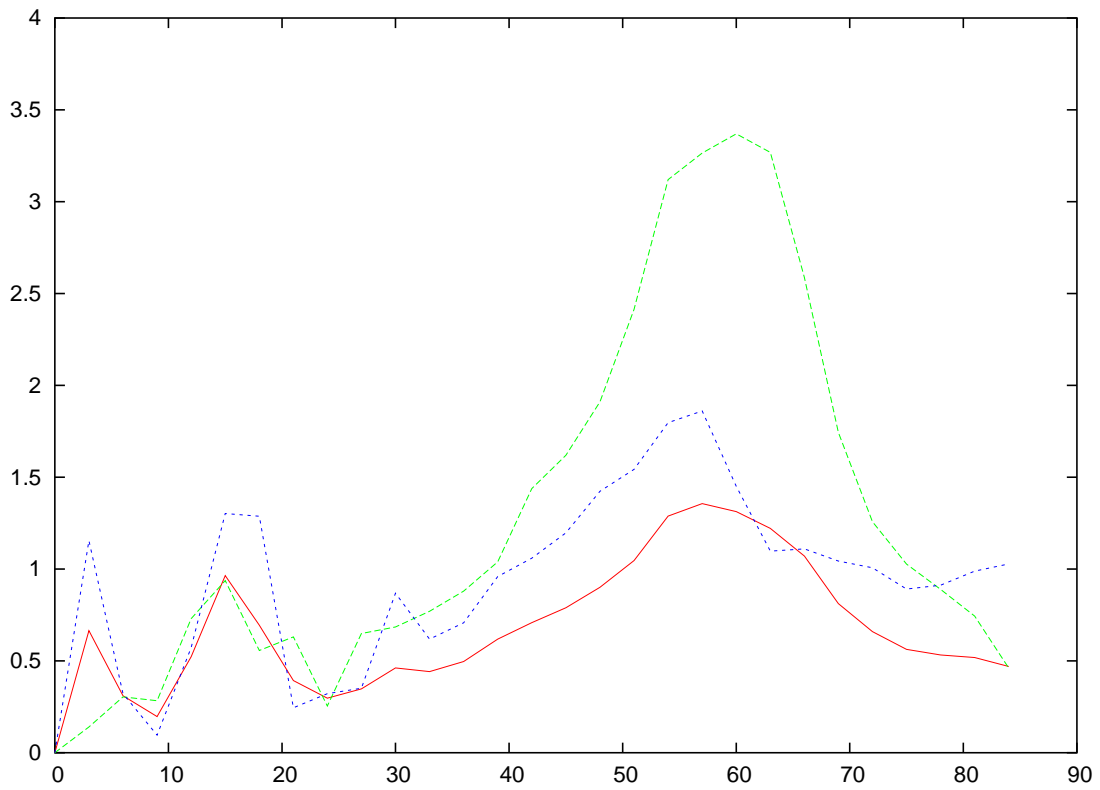


Figure 15: Area-averaged rain rate (mm hr^{-1}) within 600 km of the TC remnant versus time (hr) on Grid 2 for the 10S25E simulation. Red indicates total area average; green indicates average over the NE quadrant, and blue indicates average over the NW quadrant.

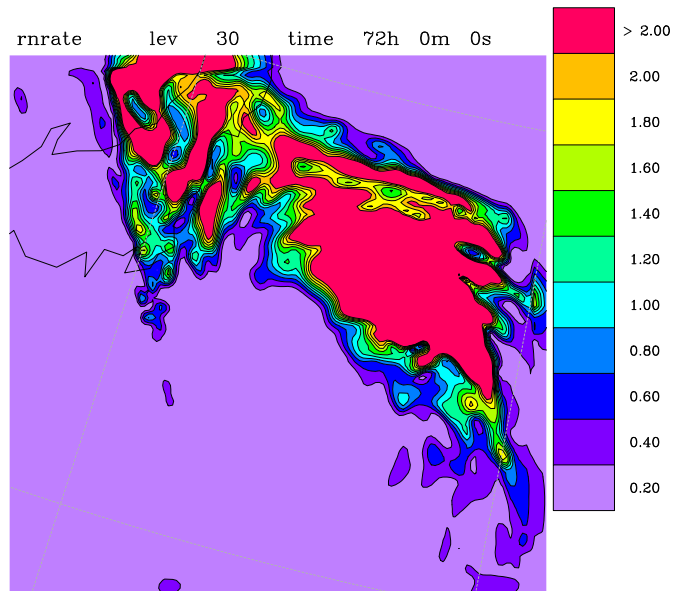


Figure 16: Same as Figure 12, but for 10S35E simulation on Grid 2 at 72 hr.

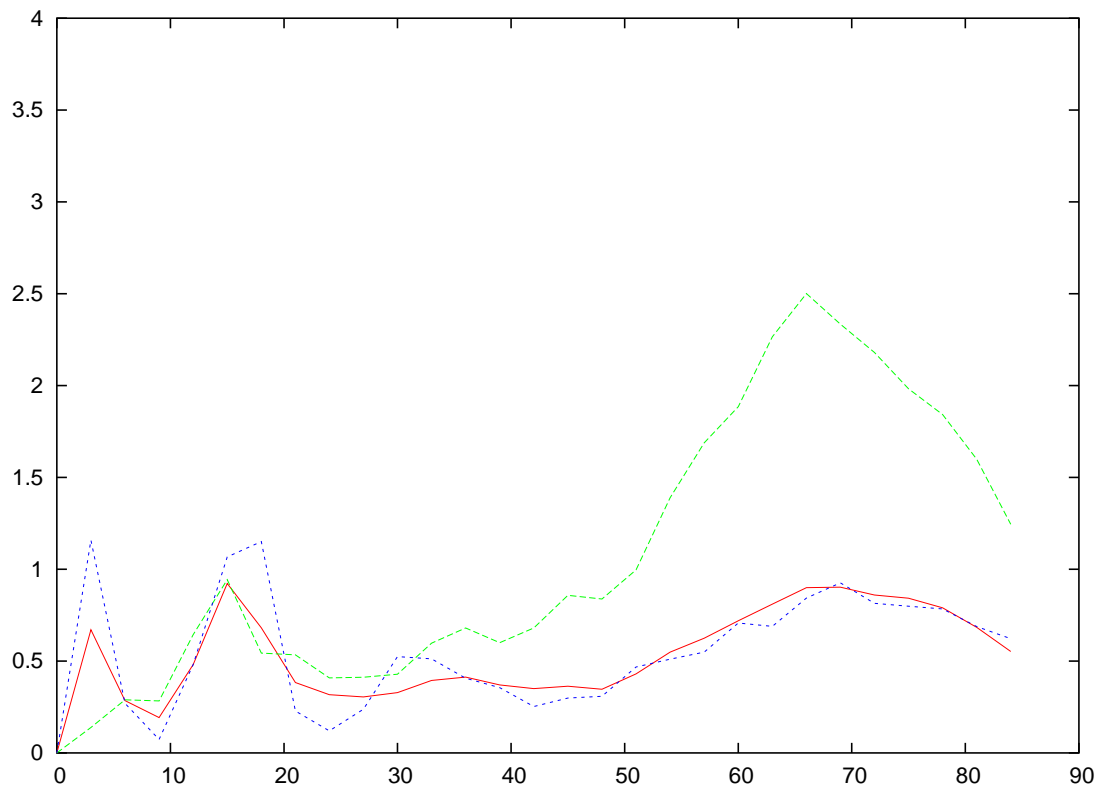


Figure 17: Same as Figure 15, but for 10S35E simulation.

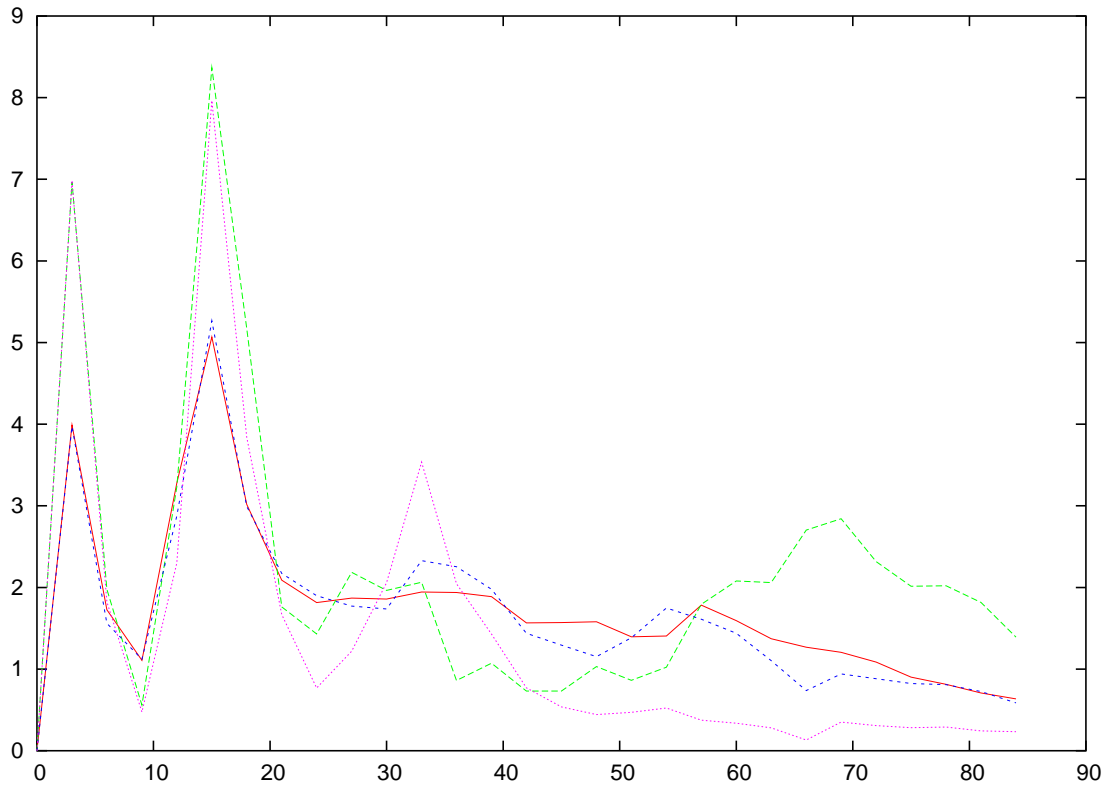


Figure 18: Area-averaged rain rate (mm hr^{-1}) within 250 km of the TC remnant versus time (hr) on Grid 3. Red indicates total area average for 10S25E case; green indicates area average over NW quadrant for 10S25E case; blue indicates total area average for 10S35E case; magenta indicates area average over NW quadrant for 10S35E case.

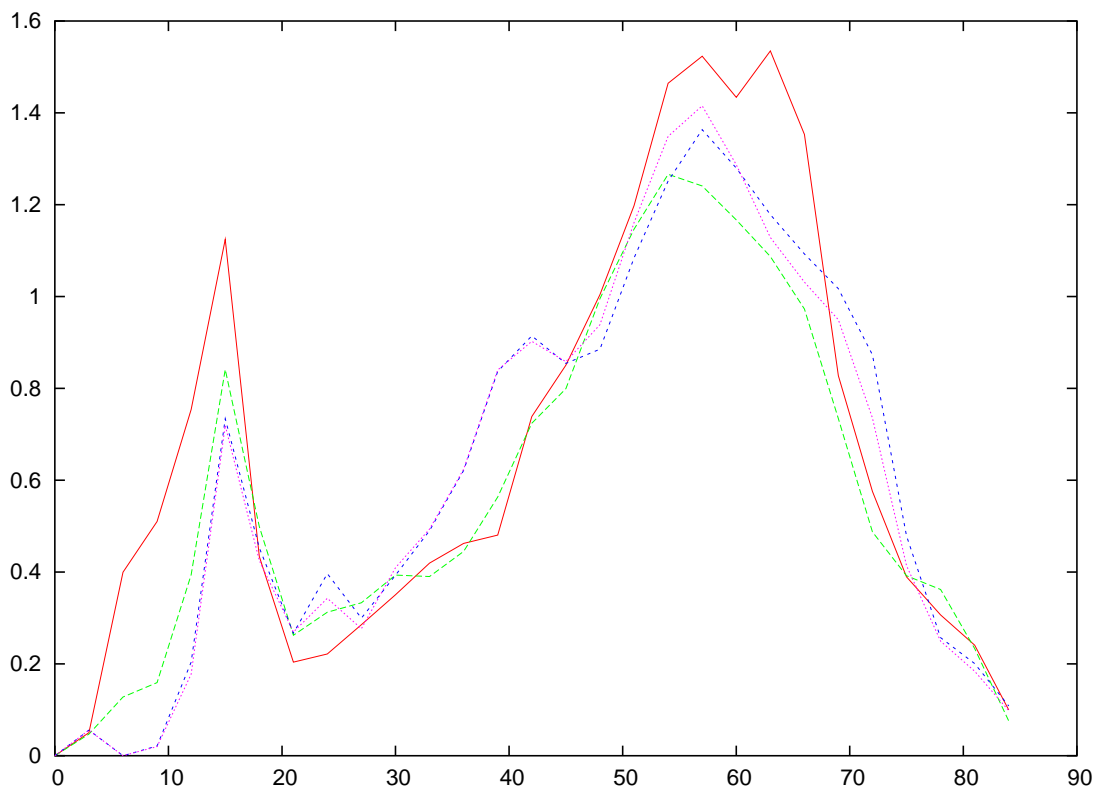


Figure 19: Area-averaged vertically-integrated snow and ice mixing ratio ($\text{g kg}^{-1} \text{ km}$) within the 600 km of the TC remnant and within the NE quadrant, versus time, for the nested 10S25E simulations. Blue indicates snow-only Grid 1; magenta indicates graupel and snow Grid 1; red indicates snow-only Grid 2; green indicates graupel and snow Grid 2.

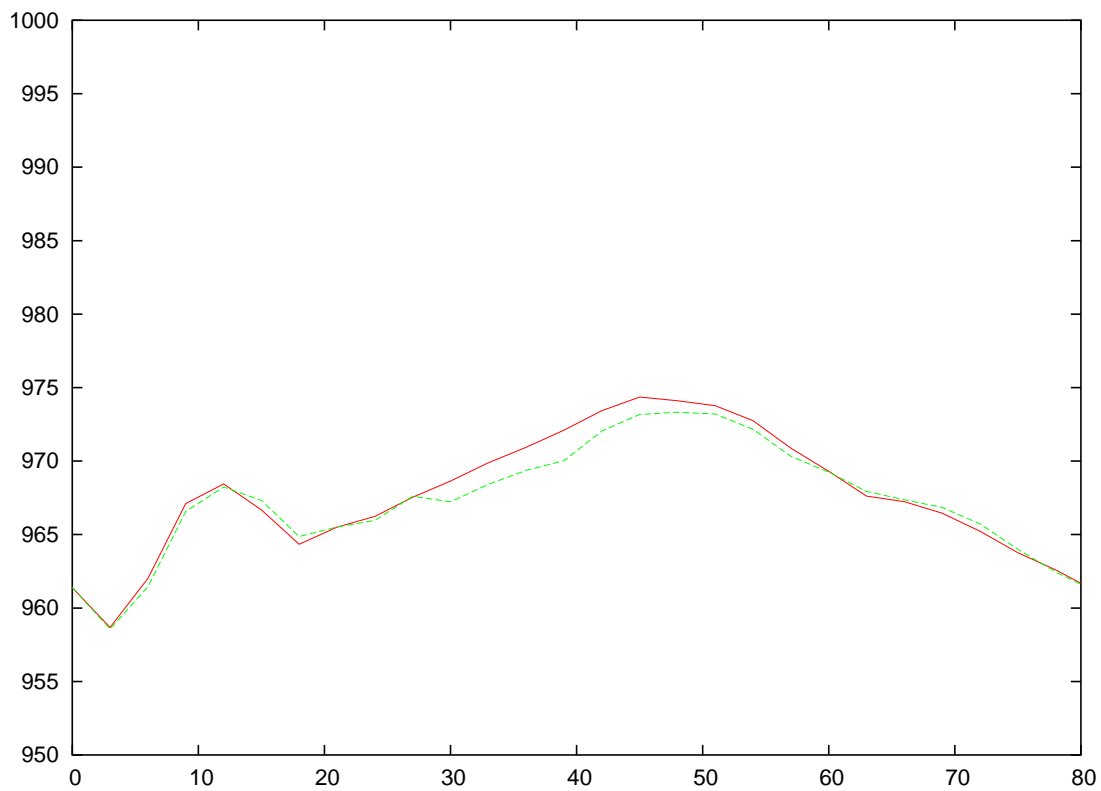


Figure 20: Minimum surface pressure of TC remnant vs. time (hr) for Grid 3 for the snow (red) and graupel (green) 10S25E simulations.